Journal of Biomedical Optics

SPIEDigitalLibrary.org/jbo

Vibrational spectroscopy and microscopic imaging: novel approaches for comparing barrier physical properties in native and human skin equivalents

Guo Yu
Guojin Zhang
Carol R. Flach
Richard Mendelsohn

SPIE

Vibrational spectroscopy and microscopic imaging: novel approaches for comparing barrier physical properties in native and human skin equivalents

Guo Yu,[a] Guojin Zhang,[b] Carol R. Flach,[a] and Richard Mendelsohn[a]
[a]Rutgers University, Department of Chemistry, 73 Warren Street, Newark, New Jersey 07103
[b]Ashland Specialty Ingredients, Global R & D, Material Science Group, 1361 Alps Road, Wayne, New Jersey 07470

Abstract. Vibrational spectroscopy and imaging have been used to compare barrier properties in human skin, porcine skin, and two human skin equivalents, Epiderm 200X with an enhanced barrier and Epiderm 200 with a normal barrier. Three structural characterizations were performed. First, chain packing and conformational order were compared in isolated human stratum corneum (SC), isolated porcine SC, and in the Epiderm 200X surface layers. The infrared (IR) spectrum of isolated human SC revealed a large proportion of orthorhombically packed lipid chains at physiological temperatures along with a thermotropic phase transition to a state with hexagonally packed chains. In contrast, the lipid phase at physiological temperatures in both porcine SC and in Epiderm 200X, although dominated by conformationally ordered chains, lacked significant levels of orthorhombic subcell packing. Second, confocal Raman imaging of cholesterol bands showed extensive formation of cholesterol-enriched pockets within the human skin equivalents (HSEs). Finally, IR imaging tracked lipid barrier dimensions as well as the spatial disposition of ordered lipids in human SC and Epiderm 200X. These approaches provide a useful set of experiments for exploring structural differences between excised human skin and HSEs, which in turn may provide a rationale for the functional differences observed among these preparations.
[DOI: 10.1117/1.JBO.18.6.061207]

Keywords: confocal Raman microscopy; human skin equivalent; infrared imaging; skin barrier structure.

Paper 12563SS received Aug. 29, 2012; revised manuscript received Oct. 15, 2012; accepted for publication Oct. 16, 2012; published online Nov. 19, 2012.

1 Introduction

Human and animal skin provide important experimental substrates for research and testing applications in the biomedical, pharmacological, and cosmetic worlds, but the continuing use of these materials for testing purposes is becoming progressively constrained. Although excised human skin is ideal for such studies, ethical considerations restrict its availability. As discussed elsewhere,[1] animal skin has, until recently, been extensively used as an alternative. Two current impediments limit the use of animal skin. From the ethical side, the 2009 EU Directive 76/768/EEC effectively eliminates animal testing in the cosmetic industry by imposing bans (a) on testing finished cosmetic products and ingredients on animals and (b) on marketing finished cosmetic products that either have been tested in animals or that contain ingredients that have been tested in animals. In addition to the ethical issues, the transferability of conclusions drawn from animal skin experiments to human skin is problematic.[2–4]

Given the above impediments to the usage of excised skin, *in vitro* models are rapidly becoming the most widely used replacements for human and animal skin testing. As such, methods characterizing their biological and physical properties must be generated and evaluated. Thus, in Article 4a of the aforementioned directive, it is noted that "Member states shall prohibit (a) the marketing of cosmetic products where the final formulation . . . has been the subject of animal testing using a method other than an alternative method after such alternative method has been validated . . ."

To begin to satisfy the EEC requirements, *in vitro* methods for monitoring penetration of exogenous materials into human skin equivalents (HSEs) have begun to be evaluated. To cite a single example from the many available, Wagner et al.[5] proposed two *in vitro* cutaneous test systems for determination of permeation and penetration parameters, utilizing the Franz diffusion cell for the former and the Saarbruecken permeation model for the latter. More recently, Netzlaff et al.[1] evaluated several models of human epidermis for morphology and for their suitability for monitoring phototoxicity, irritancy, corrosivity, and transport. These authors concluded that "the barrier function of these reconstructed human epidermis models appears to be much less developed compared to native skin".

Since the molecular structure of the barrier in reconstituted skin evidently controls its transport functions, biophysical investigations of skin molecular organization should be useful in the development of improved, targeted designs of HSEs for particular purposes. Toward this end, imaging technologies are obviously required. As noted by Brohem et al.,[6] standard monolayer two-dimensional (2-D) cell cultures cannot duplicate the architecture of skin; the need for *in vitro* three-dimensional (3-D) skin models is therefore clear. Technologies providing molecular structure information are anticipated to be useful for effective comparisons between reconstituted and excised human skin.

Address all correspondence to: Richard Mendelsohn, Rutgers University, Department of Chemistry, 73 Warren Street, Newark, New Jersey. Tel: 973-353-5613; Fax: 973-353-1264; E-mail: mendelso@andromeda.rutgers.edu

Conventional biophysical molecular structure techniques such as x-ray diffraction and electron and related microscopies as well as optically based imaging technologies such as optical coherence tomography have been profitably applied to characterize HSEs.[7–9] Each approach has advantages and limitations. X-ray diffraction-based methods[10–14] are most useful for detection of well-ordered (lipid) lamellar phases, but are not well suited for disordered and otherwise unstructured (e.g., protein containing) phases. Electron microscopy-based methods offer superb spatial resolution,[10,15] but generally require substantial specimen preparation, which may alter molecular structures. Visible and fluorescence microscopy-based approaches provide no molecular structure information.

Within the set of techniques based on optical spectroscopy/microscopy, infrared (IR) and Raman spectroscopies provide molecular structure information for characterization of the skin permeability barrier, including details about lipid packing and chain conformational order. The elucidation of structures of lipid models for the SC has been undertaken by several groups (cited below) in addition to our own, including academic laboratories in Leiden and Halle, and industrial laboratories in Geneva and New Jersey. In models such as the standard three-component (ceramide, fatty acid, cholesterol) systems, the use of chain-perdeuterated lipid species enhances the specificity of vibrational spectra, while not affecting structural parameters. Early examples of this approach were given by Naik et al.,[16] from this laboratory, and others.[17–20]

In addition to information arising from lipid molecules, vibrational spectra are sensitive to protein secondary structure. Lin et al.[21] used the Amide I spectral region (1615 to 1690 cm^{-1}) to track the thermally induced conversion of keratin from α to β structure in the presence and absence of permeation enhancers. We have examined the same conversion in single corneocytes[22] and have also taken advantage of this spectral region in our initial studies of wound healing.[23]

Technical advances over the past 15 years permit the acquisition of spatially resolved IR and Raman spectra. The techniques of IR microspectroscopic imaging and confocal Raman microscopy have both been applied to characterize skin at close to the diffraction limit in each instance. The interplay of spectral and structural information from these studies provides unique insight into tissue structures. Several studies have revealed the advantages of these approaches for studying the skin barrier. The Puppels laboratory demonstrated[24–27] the feasibility of acquiring both *in vivo* and *in vitro* Raman spectra of skin. This was followed[28] by studies by the same group tracking dimethyl sulfoxide (DMSO) permeation to a depth of ~120 μm through palmar SC and the determination of the concentration profiles of natural moisturizing factor (NMF) and water. This laboratory demonstrated[29] an extension of this method to pharmacological problems through a study of the spatial distribution of the enzymatic hydrolysis of a 5-FU prodrug to the drug itself in full-thickness excised skin. Finally, in a report relevant to the current discussion, Tfayli et al.[30] correlated observed Raman frequencies with tentative band assignments for an Episkin model. This work provides a useful starting point for the Raman characterization of artificial skin. The above citations indicate that vibrational spectroscopy, microscopy, and imaging are suitable approaches for a comparative evaluation of molecular structure and barrier properties in excised human skin versus HSEs.

The current work presents three types of IR and Raman experiments that compare barrier properties in excised skin with HSEs. First, chain packing and conformational order are compared in the isolated SC of human skin, porcine skin, and in two HSEs, Epiderm 200X with an enhanced barrier function, and Epiderm 200 with a standard barrier function, both from MatTek Corporation (Ashland, Massachusetts). Second, the formation of ordered lipid domains enriched in cholesterol is compared for excised human skin with the two HSEs. Finally, lipid barrier dimensions and the spatial disposition of the ordered lipids are compared in these samples. The current experiments are intended to begin to define a general set of vibrational spectral parameters for comparing the spatial and molecular properties of reconstituted skin models with native skin, which in turn may provide an explanation of functional differences among these preparations.

2 Materials and Methods

2.1 *Materials*

Porcine biopsies from Yucatan white, hairless pigs were purchased from Sinclair Research Center, Inc. (Columbia, Missouri). Human abdominal skin specimens were obtained from dermatological offices (otherwise to be discarded) with informed consent and in accordance with institutional protocols. HSE tissues, in particular, Epiderm 200X (EpD200x) and Epiderm 200 (EpD200), were purchased from MatTek Corporation (Ashland, MA).

2.2 *IR Microscopic Imaging*

Skin samples were fast frozen with liquid N_2 to preserve sample integrity by substantially limiting ice damage. Frozen samples were fixed on a metal chuck stage of a Bright/Hacker 5030 Microtome (Bright Instrument Company, Huntington, UK; Hacker Instruments, Fairfield, New Jersey) and sealed in ice. Following 5 min of stabilization at about −30°C, samples were microtomed to a thickness of 5 μm and carefully transferred to CaF_2 windows. After 30 min of air drying, IR images were acquired with a Perkin-Elmer Spotlight 300 system equipped with an essentially linear array (16 × 1) of mercury-cadmium-telluride (MCT) detector elements. Pixel size was 6.25 × 6.25 μm and the spectral resolution was 8 cm^{-1}. Two specimens of each type of HSE were microtomed and three to five images were acquired for each specimen. Images of sections of excised human skin shown herein are typical of the many (>20) specimens examined.

2.3 *Confocal Raman Microscopy*

Skin sample surfaces were cleaned several times with a cotton swab, inserted into a brass cell with the stratum corneum side up, and placed underneath a microscope coverslip that was pressed gently against the skin to ensure good optical contact. The cell-coverslip interface was sealed with clay to keep the moisture level constant.

Raman spectra were acquired with a Kaiser Optical Raman microprobe (Ann Arbor, Michigan) at a spectral resolution of 4 cm^{-1}. A solid-state diode laser (785 nm) with a power of ~7 mW at the sample was used as the excitation source and was focused to the desired depth with a 100× oil immersion objective. Backscattered light from the sample was collected with a near IR-CCD (ANDOR Technology, Belfast, Ireland, UK, Model DU 401-BR-DD). Spectra were acquired using a 60-s single exposure time, three accumulations, and cosmic

ray correction. Two specimens of each type of HSE were examined and the Raman images of excised human skin shown herein are typical of the many specimens examined as mentioned above.

2.4 *IR Spectra in Bulk Phases*

Skin was treated with 0.5% trypsin solution at the air-liquid interface for one day. The stratum corneum was then peeled off, rinsed with distilled water, and transferred to a ZnSe window. The isolation of SC samples from EpD200X required a protocol slightly different from human and pig skin samples, since there is no apparent distinctive physical property difference between the SC and epidermal layer in the samples. These samples were thus treated in the trypsin solution for two days, at which time no additional physical change could be observed (i.e., sample thicknesses after this time remained constant), and no additional tissue could be removed from the viable epidermis side by scratching with tweezers.

The isolated HSE SC was then placed on a ZnSe window. SC samples were dried under house vacuum for a day or two. A second ZnSe window was placed on top and the sample was contained in a temperature-controlled IR cell (Harrick Scientific, Ossining, New York). IR spectra of the dried SC were acquired with a Nicolet 6700 spectrometer (Thermo Electron Corporation, Madison, Wisconsin) operating with a spectral resolution of 2 cm^{-1}. Melting curves were generated from spectra acquired at temperature increments of ~3°C from 20°C to the highest desired value as noted in Fig. 1. Temperature was controlled using a circulating water bath and monitored with a thermocouple (Fisher Scientific Thermostat, Model 9001, Pittsburgh, Pennsylvania) embedded in the sample cell. All experiments were run in duplicate and typical data are shown.

2.5 *Factor Analysis of IR Images*

ISys software (version 3.1.1 from Malvern Instruments, UK) was used for IR and Raman spectral analysis and production of images. Spectral factor loadings and image planes of factor analysis scores were generated after linear baselines were applied over spectral regions of interest. Factor analysis, as detailed elsewhere,[29] is a multivariate statistical technique that reduces the dimensionality of the data by detecting patterns in the relationships between observed variables. The algorithm begins with principal component analysis (PCA) followed by a score segregation routine that seeks transformations between the PCA loadings and Beer's Law parameters in the IR or its equivalent in Raman. Factor analysis produces a set of factor loadings while factor scores depict correlations between the actual spectrum at each pixel and the factor loadings. Calculated factor loadings resemble typical spectra, although not of pure components. Thus, a factor loading will contain spectral features from chemical constituents (mostly skin lipids and proteins) that significantly contribute to the variance at sites with respective high factor scores. Three to six significant factors were observed from most data sets.

3 Results

3.1 *Bulk Phase IR Spectroscopy*

3.1.1 *Conformation-sensitive regions of lipid IR spectra*

One obviously important criterion for evaluating the function of HSEs is the structure and persistence of a permeability barrier.[10] Traditional (macroscopic) IR is used to compare SC lipid packing and chain conformational order in isolated human SC, porcine SC, and EpD200X. Two IR spectral regions sensitive to packing and structure are used for these purposes. The methylene rocking (715 to 735 cm^{-1}) contour is exquisitely sensitive to the packing motif adopted by the chains. As shown in Fig. 1(a), for SC isolated from human skin at temperatures less than ~30°C, the rocking mode frequency splits into a well-resolved doublet with peaks near 720 and 730 cm^{-1}. The presence of the higher frequency component is reliably diagnostic for orthorhombic perpendicular subcell packing of the lipid chains.[31,32] With increasing temperature, the doublet progressively collapses to a single peak at ~720 cm^{-1}, reflecting the disappearance of the orthorhombic packing motif and its likely replacement by hexagonal packing arrangements or (at higher temperatures) disordered chains. The progressive disappearance of the orthorhombic phase is tracked as a function of temperature in Fig. 2(a), in which the 730 cm^{-1} band intensity has been normalized to the skin protein Amide II mode near 1550 cm^{-1}.

In contrast to human SC, porcine SC as shown in Fig. 1(b) displays a somewhat asymmetric rocking contour with a peak at ~721 cm^{-1} and no detectable peak near 730 cm^{-1} (although the asymmetry may hint at the presence of a weak feature there at the very lowest temperatures). According to the correlations discussed above, the concentration of orthorhombically packed lipids in this tissue is diminished compared to human SC. Although the absence of an orthorhombic phase is not necessarily indicative of a substantially impaired barrier, certain functional assays in porcine skin indeed suggest a less efficient barrier than in human SC.[2–4] Results similar to porcine skin

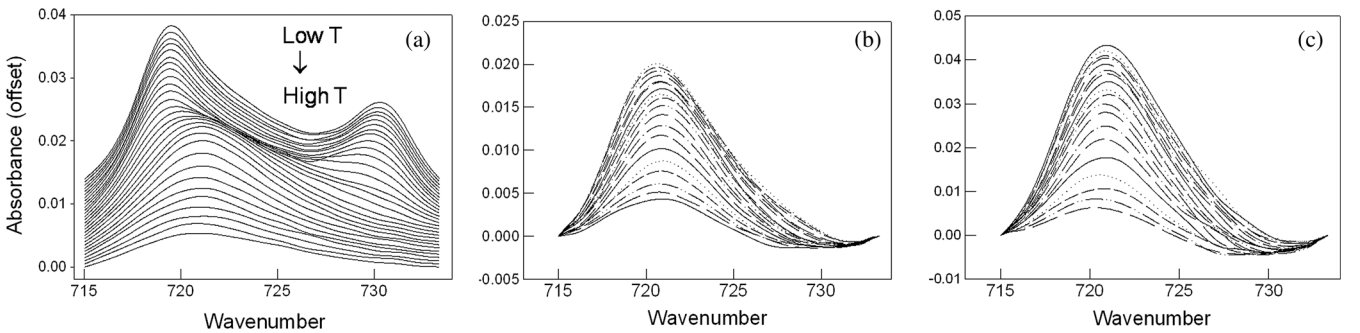

Fig. 1 Stacked absorbance plots of the methylene rocking region (715 to 733 cm^{-1}) from (a) isolated human stratum corneum as the temperature is progressively increased from 18°C to 104°C going from top to bottom; (b) isolated porcine stratum corneum spectra were acquired from 20°C to 72°C; and (c) barrier enhanced EpD200X stratum corneum from which spectra were acquired from 20°C to 72°C.

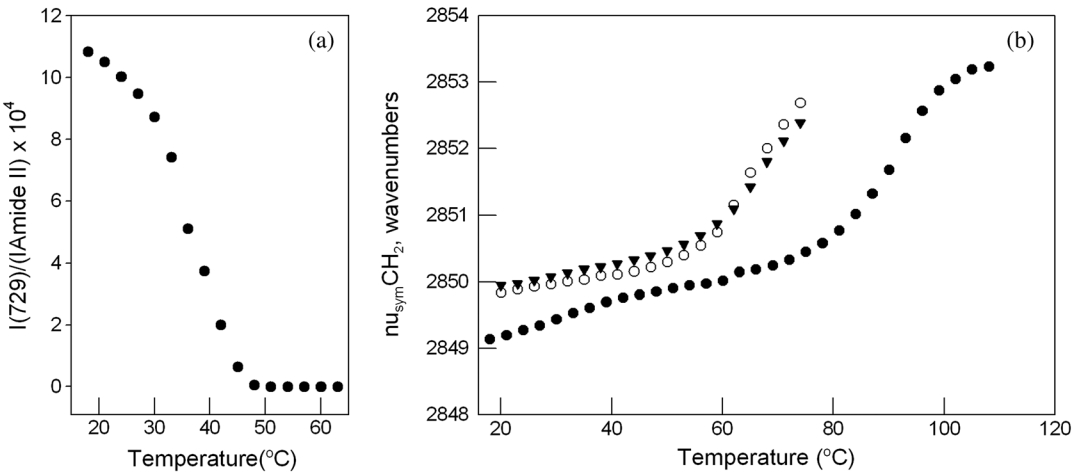

Fig. 2 (a) Temperature dependence of the area of the 729 cm^{-1} band arising from the orthorhombic phase in human SC as the temperature was increased as shown. The band intensity was normalized to the intensity of the Amide II mode in the spectrum. (b) Temperature dependence of the CH_2 symmetric stretching frequency for human SC (•), EpD200X SC (○), and porcine SC (▼).

are noted [Fig. 1(c)] for EpD200X, including a slight inflection near 730 cm^{-1} in the lowest temperature spectrum again, possibly hinting at the presence of a very small proportion of orthorhombically packed structures.

The methylene symmetric ($\upsilon_{sym}CH_2$, 2845 to 2855 cm^{-1}) and asymmetric ($\upsilon_{asym}CH_2$, 2914 to 2928 cm^{-1}) stretching bands have also proven useful for characterization of lipid assemblies. As is well known,[33] the frequencies of these modes are sensitive primarily to changes in chain intramolecular conformational order (*trans-gauche* isomerization). As an example of the utility of this spectral region, the temperature dependence of $\upsilon_{sym}CH_2$ is plotted in Fig. 2(b) for SC isolated from human excised skin, porcine SC, and EpD200X. Two transitions are evident for the human SC sample. The hexagonal → disordered (L_α) transition beginning at ~70°C and terminating at ~95°C to 100°C is accompanied by a frequency increase of 3.4 cm^{-1}, from ~2850 to 2853.4 cm^{-1}. This increase defines the progressive formation of a highly disordered lipid structure, with a final frequency similar to that observed in L_α phase of phospholipids.[33] The second broad transition from ~20°C to 40°C, detected by a significantly smaller frequency increase from ~2849.2 to 2849.7 cm^{-1}, reflects the orthorhombic-to-hexagonal packing transition previously detailed from the rocking mode contour in Figs. 1(a) and 2(a). This small increase indicates that the chains remain conformationally ordered in both phases.

The situation is markedly different for the porcine SC and EpD200X samples compared to human SC. For the porcine and HSE samples, the main lipid order → disorder transition is noted [Fig. 2(b)] at much lower temperatures (~50°C to 70°C) than in human SC. The lipid phase at low temperatures in porcine and in EpD200X SC is characterized by conformationally ordered chains but also by the absence of significant levels of orthorhombic subcell packing. While there is no direct IR marker for hexagonally packed phases in the SC, the transitions noted above are consistent with their occurrence. From a functional viewpoint, the permeability barriers presented by orthorhombic versus hexagonally packed phases are likely to be quite different. Orthorhombic phases are characterized by rigid chains locked into a highly ordered packing motif while hexagonal phases are suggested from NMR studies[34] of polyethylene to undergo rapid rotational motion about their long axes. One might anticipate that the barrier to permeability is enhanced in lipid lamellae containing orthorhombic phases, if all other factors are assumed equal. However, as shown by Ponec et al.,[10] other factors (e.g., lipid composition) evidently play a role in barrier properties. It is nevertheless clear that the IR parameters described above provide a useful biophysical characterization of lipid packing and structure within the skin barrier.

3.2 *Confocal Raman Microscopic Determination of Skin Properties*

To supplement skin barrier packing information, evaluation of spatial heterogeneity in lipid composition or chain order is possible via an approach whereby spatially resolved structural information may be generated. We illustrate the utility of confocal Raman microscopy to address this issue.

As noted earlier, confocal Raman microscopy permits acquisition of spectra with a spatial resolution of 1 to 2 μm in the lateral dimension and ~3 μm in the direction perpendicular to the SC surface. An inherent experimental problem with this technology is the single-beam nature of the experiment. When carried out in an environment such as skin in which the refractive index changes unpredictably, relative concentration information cannot be directly inferred from peak

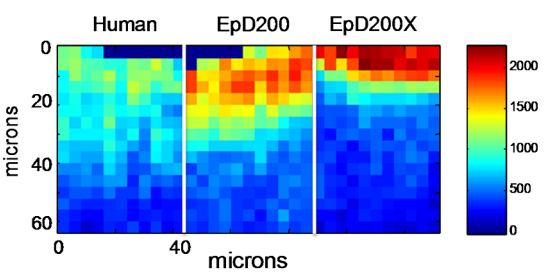

Fig. 3 Development of a Raman intensity standard. The area of the 1004 cm^{-1} band arising from the ring breathing mode of protein Phe residues is plotted as a function of position for samples of full-thickness excised human skin, EpD200, and EpD200X. Spectra were acquired over a 2-D image plane every 4 μm to a depth of 60 μm as shown. The vertical scale bar is color coded for values of Raman scattering intensity as shown on the righthand panel.

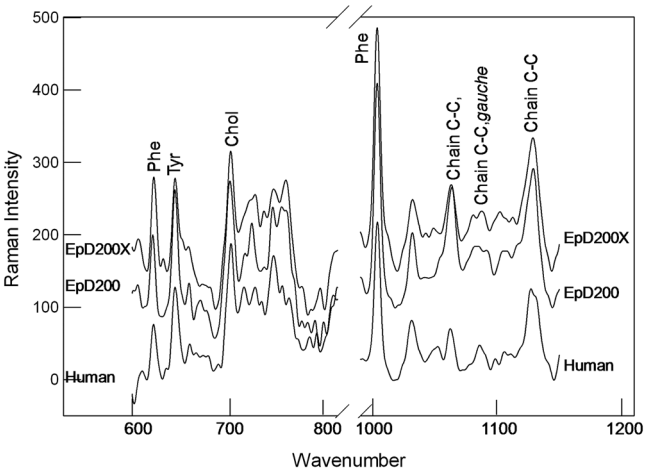

Fig. 4 Raman spectral data from the SC of the samples indicated. Some assignments of the various spectral features are given. The intensities in the 600 to 810 cm^{-1} region have been multiplied by a factor of 3 compared to those in the 990 to 1150 cm^{-1} region.

intensities. The measured intensities must be corrected for scattering efficiency changes as the excitation source samples sites at increasing depths within the tissue. Our approach to this problem (Fig. 3) is based on the observation that in skin samples studied to date, the intensity of the Phe ring stretching vibration at 1004 cm^{-1} decays mostly monotonically with depth from the skin surface. The assumption required to utilize the 1004 cm^{-1} to normalize the scattering intensities is that the concentration of Phe residues from skin proteins is constant with depth.

With this assumption, the diminution in 1004 cm^{-1} peak intensity as the excitation laser is focused progressively deeper in the tissue is presumed to arise completely from scattering losses (i.e., the inability of Raman photons from deep in the tissue to reach the detector) rather than concentration variations. The type of data acquired routinely is shown in Fig. 3 for full-thickness excised human skin, EpD200, and barrier-enhanced EpD200X, respectively. The intensity of the 1004 cm^{-1} band as a function of depth shows similar trends in each case, i.e., diminution with depth is more or less monotonic, but the magnitude of the effect varies from sample to sample. The vertical depth to which the variation in scattering intensity is considered reasonable (i.e., is not affected greatly by noise) occurs at a depth of 50 μm for human skin and EpD200 and 40 μm for the EpD200X sample. We assume the more conservative (latter) value for the following.

The utility of confocal Raman microscopy for characterizing lipid domains in skin is depicted in Figs. 4 and 5. Typical spectra collected from the SC of excised human skin, EpD200, and EpD200x over the range 580 to 810 and 990 to 1150 cm^{-1} are shown in Fig. 4. Features of interest are (1) the 701 cm^{-1} band arising from cholesterol,[22] (2) the 1004 cm^{-1} Phe band discussed previously, and (3) two chain C—C stretching modes near 1063 and 1130 cm^{-1} whose origins[35] are as follows: The 1000 to 1150 cm^{-1} region contains skeletal vibrations in which alternate carbon atoms move in opposite directions. These "skeletal optical modes" appear in ordered lipid phases as strong features from the $k = 0$ modes of an all-*trans* chain at 1130 cm^{-1} (A_g symmetry in polyethylene) and 1060 cm^{-1} (B_{1g} symmetry in polyethylene). In disordered phases a feature arises at 1080 to 1100 cm^{-1} from uncoupled C—C stretching vibrations in chain segments containing *gauche* rotations. These features are labeled in Fig. 4.

From the measured band intensities, interesting structural information may be inferred. Thus, the peak height ratio 701/1004 cm^{-1} is used to monitor cholesterol-enriched domains in the epidermis. This parameter is imaged to a depth of 40 μm in Fig. 5(a) for excised full-thickness human skin, EpD200, and EpD200X. Substantial variations in the distribution of cholesterol-enriched lipid domains are noted

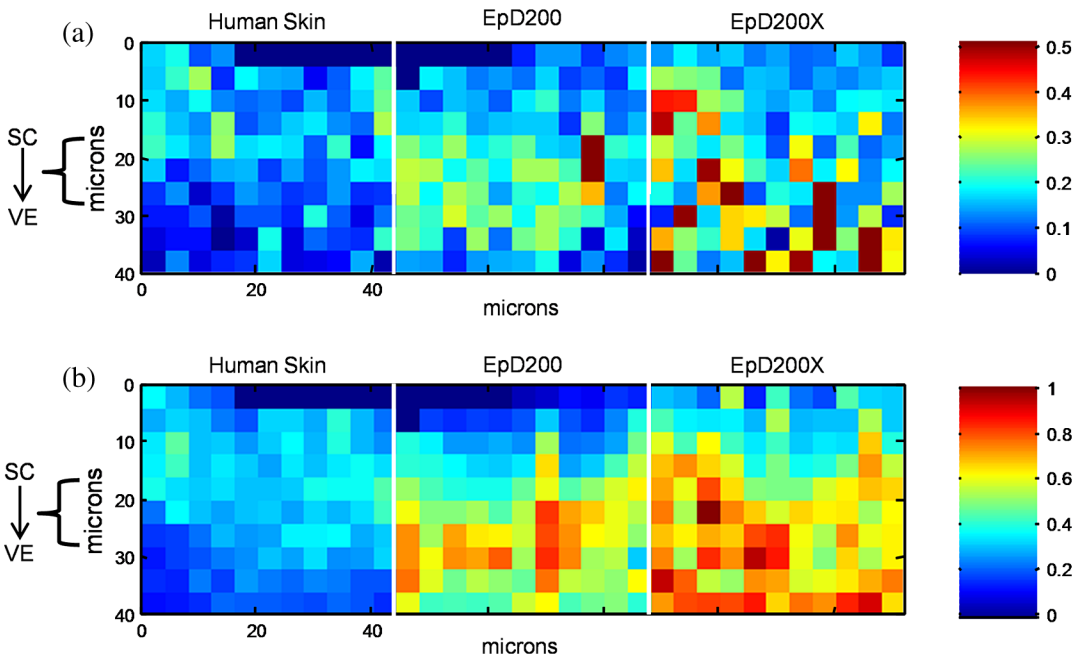

Fig. 5 (a) Spatial distribution of the area ratio of the 701/1004 cm^{-1} bands for samples of full-thickness excised human skin, EpD200, and EpD200X as marked. This ratio provides a measure of the occurrence of lipid pockets enriched in cholesterol. See text for details. (b) Spatial distribution of the area ratio of the 1063/1004 cm^{-1} bands for samples of human skin, EpD200, and EpD200X as shown. This ratio provides a measure of the occurrence of ordered lipid phases, since the 1063 cm^{-1} band arises from a particular vibration of all-*trans* lipid chains.

between these materials and reveal the presence of many more cholesterol-enriched lipid pockets in the EpD200X samples. In contrast, excised human skin shows lower relative cholesterol levels generally and many fewer pockets. EpD200 reveals intermediate levels of these structural elements. We note that the delineation of the SC and viable epidermis (VE) boundary as shown in Fig. 5(a) pertains primarily to human skin. These two regions of the tissue are difficult to distinguish spectroscopically in the HSEs.

Further insight into domain formation is evident from plots in Fig. 5(b) of the 1063/1004 cm^{-1} peak intensity ratios. Significant differences are again observed in this parameter between the samples. Pockets of a relatively higher concentration of conformationally ordered lipid are observed between depths of 15 and 40 μm for the EpD200X and between 20 and 35 μm for the EpD200. In contrast, the confocal Raman image of full-thickness excised human skin shows less variability in the concentration range of ordered lipid, with the higher concentrations appearing throughout the SC. Quantitatively, the level of ordered lipids in the HSE pockets is approximately twice that observed in the human SC. From this experiment, the Raman imaging approach is shown to provide unique information about cholesterol-enriched pockets and the distribution of conformationally ordered lipid in both SC and epidermal regions.

3.2.1 *Comparative IR microscopic imaging of excised human skin and Epiderm 200X*

Compared with confocal Raman measurements, IR imaging permits the convenient sampling of substantially larger areas, up to several mm^2. This gain is partly due to worse spatial resolution at the longer wavelengths involved in the IR measurement compared with Raman microscopy. A disadvantage of IR is that confocal measurements are not possible due to the transmission-based nature of the experiment. On the positive side, spectral S/N ratios are significantly higher in the IR compared with the Raman measurement.

The utility of IR imaging for comparison of full-thickness excised human skin with HSE is shown in Figs. 6 and 7 in which the results of factor analysis for EpD200X and human skin are depicted for two spectral regions, namely the C—H stretching region (2800 to 3000 cm^{-1}) in Fig. 6, and the 1180 to 1480 cm^{-1} region in Fig. 7. Primary IR spectral data from these samples were concatenated prior to the application of factor analysis. Six significant factor loadings (labeled F1 to F6 in the right panel of each figure) were observed in each spectral region. The score plots derived from each are labeled F1 to F6 on the left side of the lefthand figure in each instance. In Fig. 6, the spectral-like features depicted in the loadings are assigned as follows: ~2850 and ~2920 cm^{-1}, lipid methylene

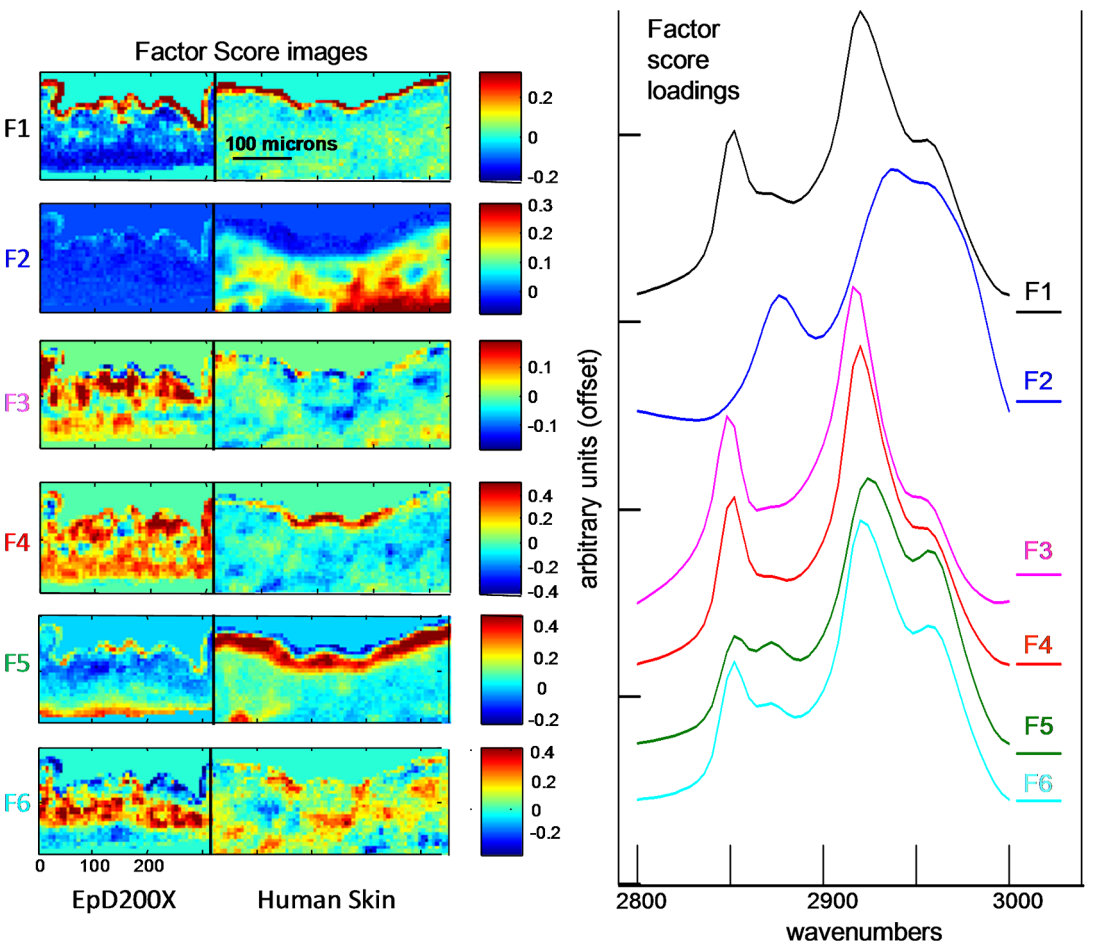

Fig. 6 Factor loadings and score images for the C—H stretching region (2800 to 3000 cm^{-1}) of full-thickness excised human skin and EpiD200X. The original IR imaging data were concatenated and factor analysis was then undertaken. Six significant loadings labeled F1 to F6 were extracted from the data and are depicted (overlaid) in the righthand panel. The scores from each loading are plotted in the lefthand panel as labeled for both human skin and the HSE.

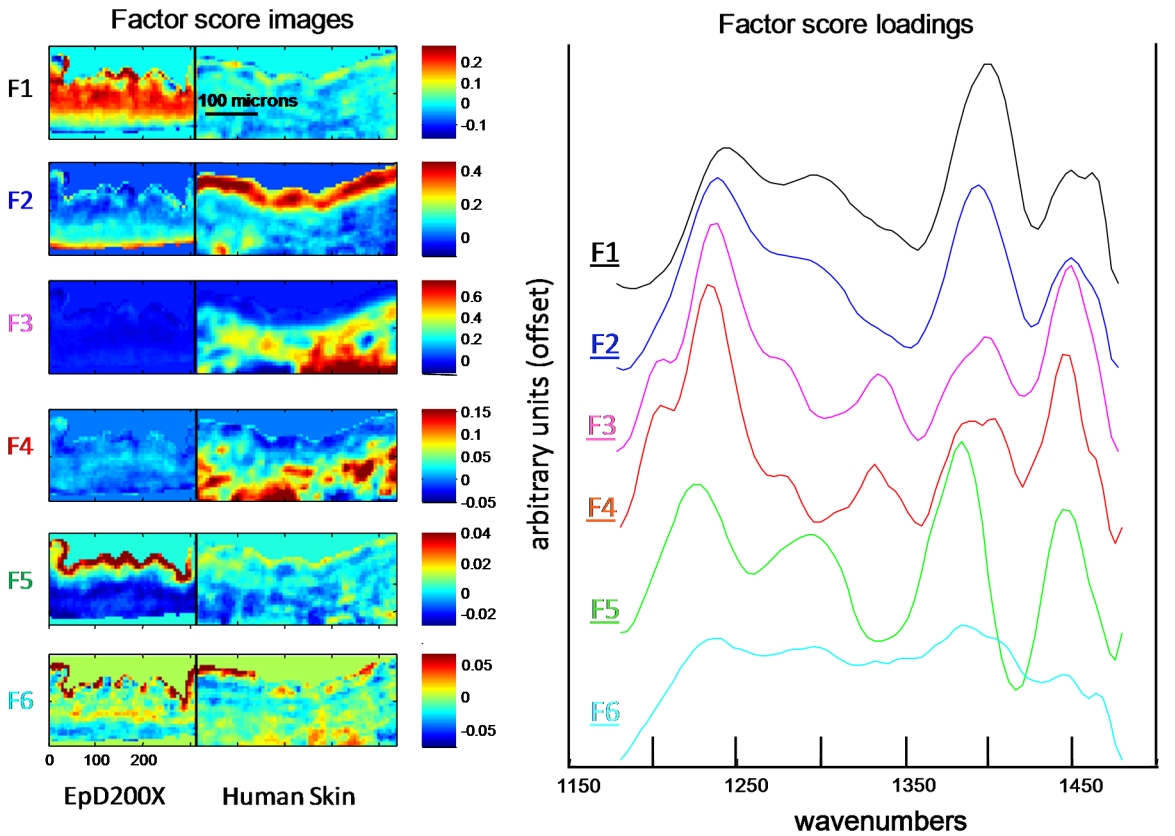

Fig. 7 Factor loadings and score images for the 1180 to 1480 cm^{-1} region of full-thickness excised human skin and EpD200X. The same data set was used as in Fig. 6. Six significant loadings labeled F1 to F6 were extracted from the data and are depicted (overlaid) in the right hand panel. The scores from each loading are plotted in the lefthand panel as labeled for both human skin and the HSE.

symmetric and asymmetric stretching modes; ~2873 cm^{-1}, protein symmetric CH_3 stretching.

As in the confocal Raman images, the main value of IR imaging arises because the spatial distribution of the chemical and structural information inherent in the spectra are exposed. As such, factor loadings can be used to identify the main chemical contributors to the variance at particular regions in the score plots of particular factors. The color coding schemes in Figs. 6 and 7 are used to define the relative contribution of each factor to a particular pixel in each plot. These are in the progressively diminishing sequence red > orange > yellow > green > blue > purple depicted in the color bars adjacent to each image. We now consider the structural ramifications of the variances detected.

The factor F1 in Fig. 6 depicts a reasonably ordered lipid population ($\upsilon_{sym}CH_2 = 2851.7\ cm^{-1}$) with very little protein, as deduced from the low IR intensity of protein methyl stretching modes. The vertical dimension of the SC layer in the F1 factor score image perpendicular to the skin surface in each tissue is ~3 pixels (~20 μm), and corresponds to the anticipated thickness of this layer.

Factor loading F2 (Fig. 6), with high scores in human skin and no counterpart in EpD200X, arises from a protein-rich loading with little detectable lipid as deduced from the absence of a lipid feature near 2850 cm^{-1} and the presence of an intense feature at 2877 cm^{-1}. The protein is readily identified as collagen both from the characteristic shape of its Amide I contour[23] (spectral data not shown here) and from the presence of the 1338 cm^{-1} band characteristic[36] of collagen 4-hydroxyproline (hyp) residues shown in factor loadings F3 and F4 (human skin) in Fig. 7. In this instance, the molecular structure information in the loading (F3 in Fig. 7) and the similarity in the score plots between F2 in Fig. 6 and F3 in Fig. 7 confirm the imaged species as collagen, mostly in the dermal region. Since EpD200X is created from keratinocytes, no collagen is anticipated in this HSE.

Two additional factors in Fig. 6, F3 and F4, depict conformationally ordered lipid chains with methylene frequencies of 2849.2 and 2851.2, respectively. These lipids are spatially distributed in the viable epidermal (VE) region of EpD200X, which is not normally considered to possess major barrier functions. No counterparts (with similar score images) are observed for the human skin. The spatial distribution of high scores for F3 and F4 in the upper VE of EpD200X is consistent with the confocal Raman image [Fig. 5(b), right] of the relative concentration of ordered lipid (1063/1004 cm^{-1} peak intensity ratio).

In addition, a substantially disordered lipid population characterized by the factor loading F6 in Fig. 6 with a methylene symmetric stretching frequency of 2855.8 cm^{-1} is evident mostly in the lower region of the viable epidermis for both EpD200X and in the dermal and VE regions of human skin. The structural significance of this lipid is unclear, but presumably it is not likely to be involved in barrier functions.

Finally, we note the presence of very similar factor scores from F5 in Fig. 6 and F2 in Fig. 7, with suggestive spatial distributions. In human skin, the loading is concentrated in the VE. Examination of the C—H spectral region (F5 in Fig. 6), indicates a mixture of lipid and protein content as shown by the presence

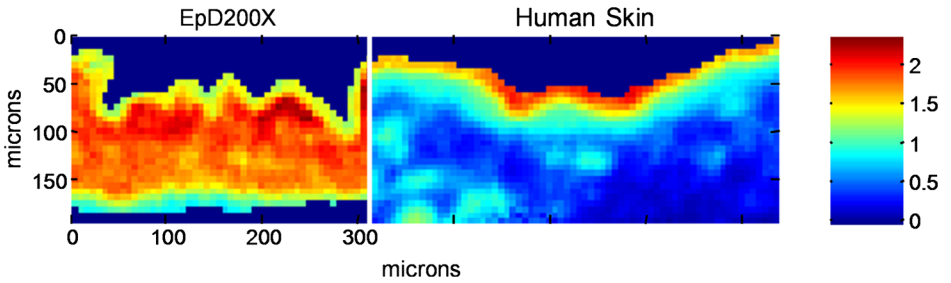

Fig. 8 Examination of the location of excess lipid in the barrier enhanced EpD200X and in excised human skin using a simple univariate measure. The intensity ratio (IR) (2852/2873 cm^{-1}) is imaged with color coding as shown on the righthand panel. The parameter tracks the lipid/protein ratio in the 2-D image plane.

of both 2850 and 2875 cm^{-1} spectral features, while the loading in the 1180 to 1475 cm^{-1} region (F2 in Fig. 7) shows no 1338 cm^{-1} feature, indicating the absence of collagen. The major protein contributor to the variance is thus identified as keratin. The complement to this in the HSE section appears to be present in factors F1 and F5 in Fig. 7, again with the absence of the collagen 1338 cm^{-1} band and the spatial distribution of high scores located in keratin-rich areas. Our prior studies of wound healing[23] suggest that this spectral region, in particular the intensity distribution in Amide III components, may be sensitive to different keratin types. In the HSE, the molecular origin of the high factor scores observed in the ~10-micron-thick region at the bottom of F5 in Fig. 6 and F2 in Fig. 7 is undetermined.

A drawback with factor analysis is the lack of a straightforward relationship between the intensity of a factor loading in a score image and the concentration of chemical constituents of the skin in the particular pixels of interest. Simple univariate analysis can overcome this issue as shown in Fig. 8 in which the spatial distribution of the lipid/protein ratio is presented as the 2852/2872 cm^{-1} peak height ratio. In excised human skin, the lipid content is maximized in the thin layer (~20 μm) corresponding to the SC, while in the EpD200X, the lipid layer is 70 to 100 μm thick and encompasses the entire epidermal layer.

The power and detail available from IR imaging for the characterization of HSEs is evident from these figures. The "lipid-enhanced" EpD200X reveals substantial extra lipid (shown in factors F3 and F4 in Fig. 6, and in the univariate image in Fig. 8) located in all epidermal layers in addition to the anticipated ordered lipid layer of the SC (F1 in Fig. 6). However, the relevance of the expanded spatial distribution of ordered lipid in HSE to barrier function is an interesting, albeit currently unresolved issue.

4 Discussion

4.1 *Macroscopic IR Experiments*

As is evident from Figs. 1 and 2, various spectral regions have sensitivities to different elements of molecular structure and organization. Thus, orthorhombic chain packing motifs are easily identified from the IR methylene rocking contours in Fig. 1. In applications from this laboratory utilizing this spectral parameter, we have tracked the kinetics of orthorhombic phase reformation following thermal perturbation in both isolated SC[37] and in three-component SC model systems.[38] Boncheva et al. have used similar spectral parameters with ATR-IR spectroscopic sampling *in vitro* to acquire thermotropic information from the SC in full thickness skin.[39]

The reliability of these IR spectra-structure correlations is established from comparison of our detection of orthorhombic phases in the SC with the x-ray diffraction study of Ponec et al.,[10] who observed orthorhombic phases in native (human) SC at 30°C that disappeared by 45°C, consistent with our measurements on isolated human SC (Fig. 1). In addition, they obtained wide-angle and electron diffraction results consistent with chain hexagonal packing in reconstructed tissues. The latter observation is consistent with our observations in HSE of minimal orthorhombic structure. Thus the spectra-structure correlations utilized here are not only consistent with a myriad of prior IR studies on simpler samples such as alkanes or phospholipids but agree with the Bouwstra lab x-ray studies of samples possessing full biological complexity.

4.2 *Vibrational Imaging*

Confocal Raman microscopy offers the significant advantages over other imaging approaches in that neither probe molecules nor substantial sample preparation is required. Either full-thickness skin or skin from which the dermal layer has been trimmed are each fully suitable. Confocal measurements may be acquired to a depth of ~80 μm with a "Z" resolution of ~2 to 3 μm. In contrast, IR absorption measurements preclude confocal applications and require skin samples that have been microtomed to the appropriate thickness. However, IR imaging provides some advantages for comparative characterization of skin sections. First, samples may be examined to any desired depth. As shown in Figs. 6 and 7, the conformational order of the SC lipids and disorder of the dermal lipids and the presence of collagen are easily detected. Also, as demonstrated in our initial studies of a healing wound,[23] the spatial distribution and activation of various keratin types is suggested from their distinctive characteristic spectral contours in the 1175 to 1450 cm^{-1} region.

4.3 *Vibrational Spectroscopy and Imaging as a Probe of HSE Structure*

To date, the type of structural information available from various physical measurements on HSEs have been elegantly demonstrated in several studies by the Leiden group who used a combination of histology, electron microscopy, and small angle x-ray diffraction. For example, in their relatively early study[10] of "human epidermis reconstructed on de-epidermized dermis," they observed, among other features of interest, formation of lamellar bodies, extrusion of same at the stratum granulosum/SC interface and the presence of well-ordered lamellar lipid

phases, with the SC lipids predominantly in a hexagonal sublattice. In a second investigation,[14] tissue architecture and quality of the permeability barrier were tracked in commercially available reconstructed human skin models and compared to human tissue. The same laboratory has more recently compared[40] water distribution and NMF content in HSEs and human skin and showed that the SC water level in HSEs is regulated by factors in addition to NMF. This study is relevant to issues such as desquamation, a process controlled by enzymes dependent on pH and water levels.

The above well-designed investigations provide a useful basis for comparison of native tissue with HSEs. The vibrational spectroscopy and imaging approaches described in the current work provide additional useful elements of molecular structure information. Thus, it is not possible from EM or from imaging experiments with probe molecules to detect particular protein structures or alterations in same, to characterize the spatial distribution of disordered lipid phases, nor to elucidate the presence of cholesterol-containing domains. Finally, this laboratory has recently demonstrated that IR imaging, in which Beer's law is obeyed, permits the estimation of the spatial distribution of the absolute concentration of exogenous materials in skin.[41]

In addition to the evaluation of endogenous skin constituents, IR and Raman imaging experiments permit characterization of perturbations in molecular structure induced by exogenous substances. Should drugs, permeation enhancers, or other exogenous skin additives alter the physical properties of the endogenous skin components, the inherent ability of IR and Raman spectroscopies to track molecular structure changes in response to the presence of exogenous substance confers unique advantages.

In the current proof-of-principle application, the lipid packing and chain conformational order differences observed between the isolated SC of human, porcine, and EpD200X, revealed in Figs. 1 and 2, provide a useful means to compare and contrast packing motifs in various samples. In addition, the confocal Raman data in Figs. 4 and 5 reveal the presence of extensive cholesterol-containing domains in the barrier-enhanced HSE compared to excised human skin. Finally, we learned from IR imaging (Figs. 6 and 7) that the spatial location of the enhanced lipid population in EpD200X was found to be throughout the epidermal region, leaving its relevance to skin barrier function unclear. As the level of structural information that can be acquired from vibrational imaging experiments develops, these measurements should generally provide a useful guide to the relationships between barrier structure and function within HSEs.

Although the use of IR and Raman imaging technologies to characterize reconstituted skin barriers are limited to date, there are studies in the literature suggesting that these approaches ought to be of general utility. For example, Bommannan et al.[42] utilized nonimaging ATR-IR in combination with tape stripping to evaluate the disorder of the SC intercellular lipids as a function of depth. In another application, the Puppels lab has applied Raman microscopy toward the same end.[25] These structural parameters may obviously define sample-to-sample differences in barrier function and are easily detected with current instrumentation. The current work along with the aforementioned studies demonstrates that extension of these types of measurements to HSEs is quite feasible.

5 Conclusions

In view of the constraints noted in Sec. 1 limiting the use of animal and human skin and therefore demonstrating the necessity to utilize reconstituted constructs, vibrational spectroscopy and microscopic imaging provide a useful set of molecular structure-based parameters for exploring differences between human skin and HSEs. Future studies will center around evaluation of a statistically significant set of HSEs. One goal of such studies will be to generate correlations between physical properties of the barrier deduced from vibrational imaging and biological functions of the barrier.

Acknowledgments

We thank Johnson & Johnson for generously supporting this work.

References

1. F. Netzlaff et al., "The human epidermis models EpiSkin®, SkinEthic® and EpiDerm®: an evaluation of morphology and their suitability for testing phototoxicity, irritancy, corrosivity, and substance transport," *Eur. J. Pharm. Biopharm.* **60**(2), 167–178 (2005).
2. R. L. Bronaugh, R. F. Stewart, and E. R. Congdon, "Methods for *in vitro* percutaneous absorption studies II. Animal models for human skin," *Toxicol. Appl. Pharmacol.* **62**(3), 481–488 (1982).
3. S. Andega, N. Kanikkannan, and M. Singh, "Comparison of the effect of fatty alcohols on the permeation of melatonin between porcine and human skin," *J. Contr. Release* **77**(1–2), 17–25 (2001).
4. J. A. Bouwstra et al., "Lipid organization in pig stratum corneum," *J. Lipid Res.* **36**(4), 685–695 (1995).
5. H. Wagner et al., "Interrelation of permeation and penetration parameters obtained from *in vitro* experiments with human skin and skin equivalents," *J. Contr. Release* **75**(3), 283–295 (2001).
6. C. A. Brohem et al., "Artificial skin in perspective: concepts and applications," *Pigm. Cell Melanoma Res.* **24**(1), 35–50 (2011).
7. J. Lademann et al., "Application of optical coherent tomography for skin diagnostics," *Laser Phys.* **15**(2), 288–294 (2005).
8. M. C. Pierce et al., "Advances in optical coherence tomography imaging for dermatology," *J. Invest. Dermatol.* **123**(3), 458–463 (2004).
9. A. T. Yeh et al., "Imaging wound healing using optical coherence tomography and multiphoton microscopy in an *in vitro* skin-equivalent tissue model," *J. Biomed. Opt.* **9**(2), 248–253 (2004).
10. M. Ponec et al., "Barrier function in reconstructed epidermis and its resemblance to native human skin," *Skin Pharmacol. Appl. Skin Physiol.* **14**(Suppl.1), 63–71 (2001).
11. J. A. Bouwstra et al., "Characterization of the stratum corneum structure in reconstructed epidermis by X-ray diffraction," *J. Lipid Res.* **36**(3), 496–504 (1995).
12. J. A. Bouwstra et al., "Phase behavior of isolated skin lipids," *J. Lipid Res.* **37**(5), 999–1011 (1996).
13. J. A. Bouwstra et al., "Characterization of stratum corneum structure in reconstructed epidermis by X-ray diffraction," *J. Lipid Res.* **36**(3), 496–504 (1995).
14. M. Ponec et al., "Lipid and ultrastructural characterization of reconstructed skin models," *Int. J. Pharm.* **203**(1–2), 211–225 (2000).
15. N. A. Monteiro-Riviere et al., "Comparison of an *in vitro* skin model to normal human skin for dermatological research," *Microsc. Res. Tech.* **37**(3), 172–179 (1997).
16. A. Naik et al., "Mechanism of oleic acid-induced skin penetration enhancement *in vivo* in humans," *J. Contr. Release* **37**(3), 299–306 (1995).
17. D. J. Moore, M. E. Rerek, and R. Mendelsohn, "FTIR spectroscopy of the conformational order and phase behavior of ceramides," *J. Phys. Chem. B* **101**(44), 8933–8940 (1997).
18. A. Percot and M. Lafleur, "Direct observation of domains in model stratum corneum lipid mixtures by Raman microspectroscopy," *Biophys. J.* **81**(4), 2144–2153 (2001).
19. H-C. Chen et al., "Effect of cholesterol on miscibility and phase behavior in binary mixtures with synthetic ceramide 2 and octadecanoic acid. Infrared studies," *Biochim. Biophys. Acta* **1512**(2), 345–356 (2001).
20. M. E. Rerek et al., "FTIR spectroscopic studies of lipid dynamics in phytosphingosine ceramide models of the stratum corneum lipid matrix," *Chem. Phys. Lipids* **134**(1), 51–58 (2005).

21. S. Y. Lin, K. J. Duan, and T. C. Lin, "Microscopic FT-IR/DSC system used to simultaneously investigate the conversion process of protein structure in porcine stratum corneum after pretreatment with skin penetration enhancers," *Methods Find. Exp. Clin. Pharmacol.* **18**(3), 175–181 (1996).
22. G. Zhang et al., "Vibrational microscopy and imaging of skin: from single cells to intact tissue," *Anal. Bioanal. Chem.* **387**(5), 1591–1599 (2007).
23. K. L. A. Chan et at., "A coordinated approach to cutaneous wound healing: vibrational microspectroscopic imaging and molecular biology," *J. Cell. Mol. Med.* **12**(5B), 2145–2154 (2008).
24. P. J. Caspers et al., "*In vivo* confocal Raman microspectroscopy of the skin: noninvasive determination of molecular concentration profiles," *J. Invest. Dermatol.* **116**(3), 434–442 (2001).
25. P. J. Caspers, G. W. Lucassen, and G. J. Puppels, "Combined *in vivo* confocal Raman spectroscopy and confocal microscopy of human skin," *Biophys. J.* **85**(1), 572–580 (2003).
26. T. C. Bakker Schut et al., "Real-time tissue characterization on the basis of *in vivo* Raman spectra," *J. Raman Spectrosc.* **33**(7), 580–585 (2002).
27. M. Boncheva et al., "Depth profiling of Stratum corneum hydration *in vivo*: a comparison between conductance and confocal Raman spectroscopic measurements," *Exp. Dermatol.* **18**(10), 870–876 (2009).
28. P. J. Caspers et al., "Monitoring the penetration enhancer dimethyl sulfoxide in human stratum corneum, *in vivo* by confocal Raman microscopy," *Pharm. Res.* **19**(10), 1577–1580 (2002).
29. G. Zhang et al., "Imaging the prodrug-to-drug transformation of a 5-fluorouracil derivative in skin by confocal Raman microscopy," *J. Invest. Dermatol.* **127**(5), 1205–1209 (2007).
30. A. Tfayli et al., "Molecular characterization of reconstructed skin model by Raman microspectroscopy: comparison with excised human skin," *Biopolymers* **87**(4), 261–274 (2007).
31. R. G. Snyder, "Vibrational correlation splitting and chain packing for the crystalline n-alkanes," *J. Chem. Phys.* **71**(8), 3229–3235 (1979).
32. R. G. Snyder, "Vibrational spectra of crystalline n-paraffins. Part II. Intermolecular effects," *J. Mol. Spectrosc.* **7**(1–6), 116–144 (1961).
33. R. Mendelsohn and H. H. Mantsch, "Fourier transform infrared studies of lipid/protein interaction," Chapter 4 in Progress in *Protein-Lipid Interactions 2*, A. Watts and J. J. H. H. M. de Pont, Eds., pp. 103–146, Elsevier, Amsterdam, Netherlands (1986).
34. M. deLangen, H. Luigjes, and K. O. Prins, "NMR study of chain dynamics in the hexagonal high-pressure phase of polyethylene," *Polymer* **41**(3), 1193–1203 (2000).
35. R. G. Snyder, "Vibrational study of the chain conformation of the liquid n-paraffins and molten polyethylene," *J. Chem. Phys.* **47**(4), 1316–1360 (1967).
36. K. Belbachir et al., "Collagen types analysis and differentiation by FTIR spectroscopy," *Anal. Bioanal. Chem.* **395**(3), 829–837 (2009).
37. R. D. Pensack et. al., "Infrared kinetic/structural studies of barrier reformation in intact stratum corneum following thermal perturbation," *Appl. Spectrosc.* **60**(12), 1399–1404 (2006).
38. D. J. Moore et al., "Kinetics of membrane raft formation: fatty acid domains in stratum corneum lipid models," *J. Phys. Chem. B* **110**(5), 2378–2386 (2006).
39. M. Boncheva, F. Damien, and V. Normand, "Molecular organization of the lipid matrix in intact Stratum corneum using ATR-FTIR spectroscopy," *Biochim. Biophys. Acta* **1778**(5), 1344–1355 (2008).
40. J. A. Bouwstra et al., "Water distribution and natural moisturizer factor content in human skin equivalents are regulated by environmental relative humidity," *J. Invest. Dermatol.* **128**(2), 378–388 (2008).
41. G. Mao et al., "Imaging the distribution of sodium dodecyl sulfate in skin by confocal Raman and infrared microspectroscopy," *Pharm. Res.* **29**(8), 2189–2201 (2012).
42. D. Bommannan, R. O. Potts, and R. H. Guy, "Examination of stratum corneum barrier function *in vivo* by infrared spectroscopy," *J. Invest. Dermatol.* **95**(4), 403–408 (1990).